Journal of Materials Research and Technology 38 (2025) 2197–2211

Contents lists available at ScienceDirect

Journal of Materials Research and Technology

journal homepage: www.elsevier.com/locate/jmrt

Tribocorrosion behavior of nickel-free duplex and 316L stainless steels fabricated by laser powder bed fusion in artificial seawater

Abhinav Anand [a,1], Chinmayee Nayak [a,*], Ermei Mäkilä [b], Zaiqing Que [c], Heidi Piili [a], Sneha Goel [c], Antti Salminen [a], Ashish Ganvir [a]

[a] Research Group of Digital Manufacturing and Surface Engineering, Department of Mechanical and Materials Engineering, University of Turku, Finland
[b] Laboratory of Industrial Physics, Department of Physics and Astronomy, University of Turku, Turku, Finland
[c] Advanced Materials for Nuclear Energy, VTT Technical Research Centre of Finland, Finland

ARTICLE INFO

Keywords:
Laser powder bed fusion
Nickel-free duplex steel
Tribocorrosion
Seawater

ABSTRACT

In this work, nickel-free duplex stainless steel (NiFDSS) and 316L stainless steel were produced by laser powder bed fusion (PBF-LB/M) under optimized parameters, reaching 98.83 % and 99.80 % relative densities, respectively. Microstructural analysis showed transformation from fully ferritic in the as-built condition to duplex after heat treatment (950 °C/1 h, followed by water quenching) for NiFDSS. Corrosion resistance was evaluated by potentiodynamic polarization in artificial seawater (0.6 M NaCl with pH 8.2), while tribocorrosion performance was measured in a ball-on-disc setup under the same electrolyte. As-built NiFDSS exhibited a lower corrosion current density (1.30 μA/cm^2) than 316L (1.78 μA/cm^2), and heat treatment further reduced it to 0.65 μA/cm^2, reflecting enhanced corrosion resistance. Under tribocorrosion, NiFDSS and heat-treated NiFDSS maintained lower corrosion rates but incurred higher wear rates than 316L, driven by residual porosity along with cleavage-prone fragmentation in the as-built alloy and sigma-phase-assisted cracking after heat treatment. Overall, PBF-LB/M of NiFDSS provided superior corrosion resistance while exhibiting lower wear performance than 316L. Porosity control through further PBF-LB/M parameters refinement and heat-treatment optimization is required to minimize residual pores and suppress sigma-phase precipitation, thereby improving wear resistance of NiFDSS.

1. Introduction

316L austenitic stainless steel is widely favored across the marine, biomedical, food-processing, and chemical industries because of its exceptional corrosion resistance, versatility, and durability [1]. It resists rust, erosion, and pitting in seawater. However, the growing demand for materials that withstand even harsher marine and industrial conditions has drawn attention to duplex stainless steel (DSS), a family of alloys whose balanced ferritic-austenitic microstructure delivers properties unattainable in conventional austenitic grades such as 316L. In DSS, the ferrite phase, enriched with chromium and molybdenum, enhances resistance to localized corrosion, while nickel-stabilized austenite contributes mechanical strength and toughness [2,3]. This combination results in DSS having higher yield strength, better thermal conductivity, and greater resistance to chloride-induced stress corrosion cracking compared to 316L [4].

Despite these advantages, DSS is less popular than 316L due to its higher cost, which is driven by complex manufacturing processes and higher alloying content. Nickel-free duplex stainless steel (NiFDSS), developed by researchers at ETH Zurich to address these cost concerns, substitutes nickel with increased nitrogen and manganese, reducing costs while maintaining high corrosion resistance and mechanical strength [5]. This makes NiFDSS a viable and economical alternative for marine applications, offering similar or superior performance and having a 3 % lower density at a fraction of the cost of 316L [6].

1.1. PBF-LB/M in the marine sector

Advancements in additive manufacturing (AM), particularly laser-based powder bed fusion (PBF-LB/M), have impacted the marine

* Corresponding author.
E-mail address: chinmayee.nayak@utu.fi (C. Nayak).
[1] Current address: Department of Mechanical Engineering, Politecnico di Milano, Via La Masa 1, 20156 Milano, Italy; Institute of Plasma PhysicsThe Czech Academy of Sciences, Prague, Czech Republic.

https://doi.org/10.1016/j.jmrt.2025.08.070
Received 27 June 2025; Received in revised form 30 July 2025; Accepted 10 August 2025
Available online 11 August 2025

industry by enabling the precise and efficient production of complex, customized components via offering numerous advantages, including reduced lead times, cost savings, and the ability to manufacture intricate geometries that are difficult to achieve with traditional methods [7,8]. PBF-LB/M employs a high-power laser to selectively melt and consolidate successive layers of metal powder, producing fully dense parts with rapid solidification and precise microstructural control [9]. This manufacturing route is particularly suited for fabricating marine components such as heat exchangers, propeller shafts, impeller blades, and exhaust manifolds [10]. While austenitic grades have been extensively studied in PBF-LB/M, research on DSS is gaining popularity.

Salman et al. [11] studied that the as-built state of PBF-LB/M-built 316L consists of a fully austenitic phase, showing optimal mechanical performance, and annealing heat treatments (ranging from 300 to 1400 °C) caused no significant phase changes or improvement in strength and ductility. Similarly, in other studies [12,13], electron backscatter diffraction (EBSD) mapping and X-ray diffraction (XRD) analysis showed a fully austenitic structure of the as-built 316L specimens. However, DSS manufactured via PBF-LB/M consisted of a fully ferritic microstructure in the as-built state. Therefore, heat treatment must be performed to attain the duplex phase matrix and enhance corrosion resistance and mechanical behavior [14,15]. Heat treatment involving solutionizing (solution heat treatment) at 900–1100 °C, followed by quenching, was performed for DSS to obtain the duplex microstructure and to prevent the formation of embrittling intermetallic phases like sigma and chi, ensuring uniform distribution of alloying elements and maintaining corrosion resistance and mechanical properties [4]. Florian et al. [16] studied that heat treatment of PBF-LB/M-built 2205 DSS, involving solutionizing in the range of 1000–1200 °C, followed by water quenching, transformed the microstructure from fully ferritic to duplex, reducing ultimate strength but enhancing ductility. In our previous work, the first comprehensive study was conducted on PBF-LB/M-built NiFDSS, optimizing process parameter values to achieve 98.47 % relative density, and found that NiFDSS offers better biocompatibility than 316L in simulated body fluid for biomedical applications [17].

1.2. Tribocorrosion in marine environments

In marine applications, materials are frequently subjected to tribocorrosion, a phenomenon where simultaneous wear and corrosion synergistically degrade the components and impact their longevity and performance [18]. Stainless steel components have a passive oxide layer that provides corrosion resistance but can deteriorate under cracking, wear, or deformation, resulting in accelerated localized corrosion until repassivation occurs [19]. Marine environments exacerbate this issue, exposing components to saline conditions and subjecting them to abrasive wear and cyclic fatigue from tides, winds, and vessel movements [20]. This creates a tribocorrosion system, leading to material removal, surface degradation, and the gradual loss of mechanical integrity. For example, when exposed to mechanical stresses, abrasive water particles, and corrosive seawater environments, boat propeller shafts undergo tribocorrosion. Understanding the tribocorrosion behavior of materials is essential to predict their performance and ensure reliability in such an environment.

In a study by Stendal et al. [21], the tribocorrosion characteristics of PBF-LB/M-built 316L were assessed in a 0.9 wt% NaCl solution and compared with those of the wrought material. The findings indicated that the PBF-LB/M-built 316L samples demonstrated superior performance, including greater wear resistance, enhanced ability to maintain passivation, and increased resistance to pitting corrosion. Gao et al. [22] investigated the tribocorrosion performance of wrought 2205 DSS in a simulated seawater environment with a pH of 8.2. Sneha et al. [23] investigated the electrochemical behavior of PBF-LB/M processed NiFDSS in high-temperature water, revealing tunable microstructures via heat treatment and 2 to 3 times lower oxidation rates than wrought 316L. This improvement was attributed to differences in oxide-layer composition and lower nickel concentrations at the oxide interface. Recent studies on PBF-LB/M magnesium alloys further illustrated how build parameters and subsequent heat treatment govern microstructure evolution and corrosion behaviour [24,25].

Despite the increasing adoption of DSS in seawater environments, their tribocorrosion behavior, a critical factor for marine applications, remains largely unexplored when processed via PBF-LB/M. Existing studies have extensively analyzed the mechanical properties and corrosion resistance of DSSs. Still, no systematic investigation has been conducted on their tribocorrosion performance when manufactured through PBF-LB/M, leaving a critical gap in understanding their real-world durability in marine environments.

1.3. Objective of this work

To address this, the present study investigates NiFDSS, an emerging material with the potential to replace conventional 316L stainless steel, which is the most commonly used stainless-steel powder in PBF-LB/M [26]. The pitting-resistance equivalent number (PREN) is a widely used index for ranking stainless steels in a chloride environment: PREN = [Cr] + 3.3 [Mo] + 16 [N] (wt.%) [27]. Lean duplex grades such as NiFDSS evaluated in this study have a PREN value between 30 and 32, while for conventional 316 L, it is ~25. The high-alloy duplex, such as 2205 grade, approaches a PREN value of ~35. Because the NiFDSS alloy was designed to deliver 316L-level corrosion resistance or higher without nickel, 316L rather than the costlier 2205 grade, was chosen as the reference material to evaluate the advantages or disadvantages of a nickel-free steel grade while keeping powder cost comparable.

In this study, NiFDSS samples were fabricated via optimized PBF-LB/M processing, achieving near-full density. Based on the simulated phase diagram, the as-built NiFDSS was subjected to heat treatment to transform its initially ferritic structure into a duplex phase, a crucial step for improving its tribocorrosion resistance. The study evaluated the wear and corrosion performance of NiFDSS in artificial seawater (0.6 M NaCl, pH 8.2) and compared it with PBF-LB/M-fabricated 316L stainless steel, which served as the reference material. Since the tribocorrosion behavior of heat-treated 316L has been extensively studied in previous works [22–24], no additional heat treatment was applied to 316L in this study. This work represents a first-of-its-kind tribocorrosion assessment of NiFDSS processed via PBF-LB/M, providing new insights into the interplay between phase evolution, corrosion resistance, and wear performance. This study lays the foundation for their broader adoption in high-performance marine applications by bridging the knowledge gap in additively manufactured DSSs.

2. Materials and methods

2.1. Materials used

The 316L gas-atomized powders utilized in this study were sourced from SLM Solutions Group AG, while the NiFDSS gas-atomized powders were obtained from Sandvik Osprey Ltd. The chemical composition of these powders, as provided by the manufacturers, is shown in Table 1. In NiFDSS, nickel was eliminated for cost and sustainability reasons. Its austenite-stabilising role was compensated by increasing manganese and nitrogen. Molybdenum was added independently to improve localized pitting corrosion resistance by raising the PREN value.

The morphology of the powders was examined using a Thermo Scientific Apreo S field-emission scanning electron microscope (SEM). Overview micrographs of the particles and final samples were taken with an accelerating voltage of 2 kV. Elemental analysis was carried out with energy-dispersive X-ray spectroscopy (EDS) using an Oxford Instruments Ultim Max 100 EDS detector. The spectral information was collected using an accelerating voltage of 20 kV, revealing spherical particles with some surface protuberances, as shown in Fig. 1. The

Table 1
Actual chemical composition of 316L and NiFDSS powders in weight%.

Alloy	Cr	Mn	Mo	Si	N	C	S	P	Ni	O	Nb	Co	Fe
316L	17.84	0.90	2.43	0.64	0.10	0.02	0.01	0.007	12.50	0.02	–	–	Bal.
NiFDSS	17.30	11.40	3.20	0.70	0.18	0.03	0.005	0.017	0.10	0.16	0.01	0.01	Bal.

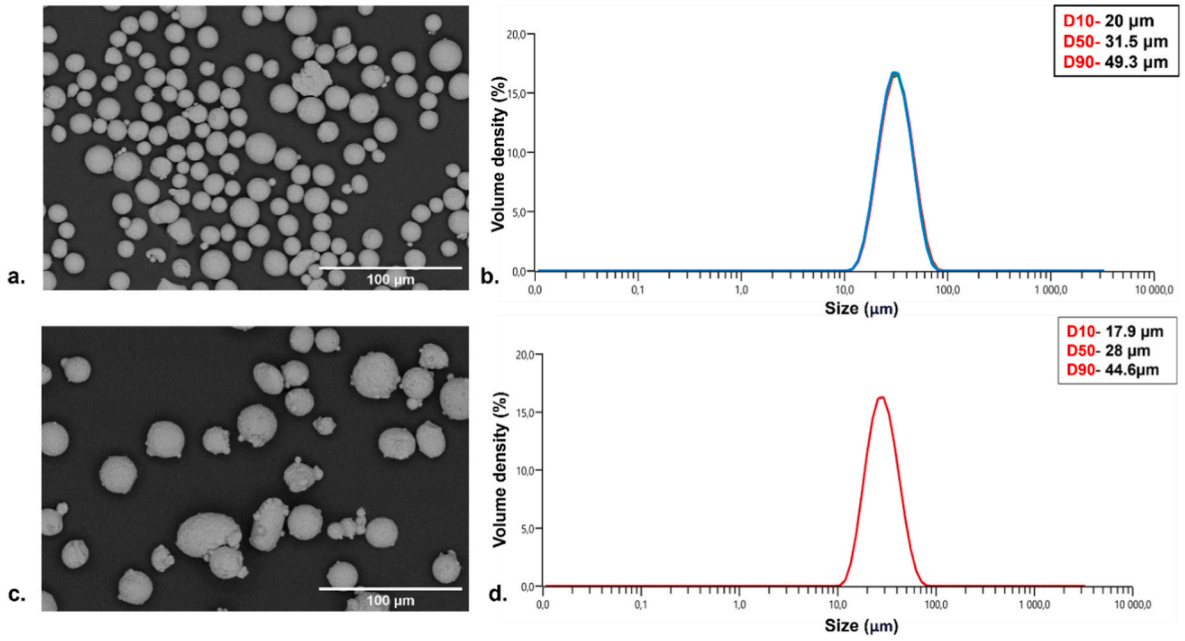

Fig. 1. High-angle backscattered electron image of (a) 316L powder, (c) NiFDSS powder; PSD curve of (b) 316L powder, (d) NiFDSS powder.

powder size distribution (PSD) was measured using laser diffraction with Malvern Mastersizer 3000. which indicated that the D10, D50, and D90 values for 316L were higher.

2.2. Sample manufacturing

NiFDSS and 316L samples were manufactured using the Aconity MIDI + machine via PBF-LB/M in this study. The system was equipped with a single SM fiber laser with a maximum power of 400 W and a 3D scanner. In our previous study [17], PBF-LB/M process parameter values for NiFDSS, i.e., laser power, scanning speed, hatch distance, and layer thickness, were optimized to 160 W, 600 mm/s, 0.08 mm, and 0.03 mm, respectively, to obtain samples of relative density 98.47 %. However, the manufactured samples showcased overmelting, distortion, and cracks formed on the edges of the specimens (refer to Fig. A1). To get a denser sample with a lower porosity %, a new design of experiment was adopted in which laser power was varied from 110 W to 160 W with a step size of 5 W. Eleven specimens with different laser powers were manufactured, and each sample underwent visual inspection, and relative density measurements were carried out to assess the porosity %. The samples were weighed in the open air and when submerged in distilled water using the Densimeter H-3000s setup. With the laser power of 140 W, scanning speed of 600 mm/s, hatch distance of 0.08 mm, and layer thickness of 0.03 mm, samples of relative density 98.83 % were produced. Please refer to Figs. A2, A3, A4, and Table A1 in Supplementary data for the design of the experiment chart, the images of the NiFDSS sample manufactured during and after process parameters optimization, and the obtained relative density % for different laser powers.

In the case of 316L, the optimized process parameter values were taken from the Aconity database, i.e., laser power of 150 W, scanning speed of 900 mm/s, hatch distance of 0.08 mm, and layer thickness of 0.03 mm. For NiFDSS and 316L, the laser beam diameter of 80 µm was used. All samples in this study were manufactured using a stripe-hatching scanning strategy. The stripes were 5 mm wide, and the scanning direction was rotated by 67° between successive layers. This approach was adopted to alter the thermal gradient direction, helping to minimize residual stress and ensure that they were evenly distributed, thereby reducing the likelihood of cracking in the parts. During the sample manufacturing, argon gas was supplied to the build chamber to maintain an oxygen concentration below 500 ppm. 316L samples were produced with a relative density of 99.80 %.

Two different types of samples were produced for various objectives in this study: the first set consisted of cylindrical samples, 15 mm in height and 30 mm in diameter, used for process parameter optimization and material characterization. The second set consisted of cylindrical discs with a diameter of 60 mm and a height of 11 mm, intended for tribocorrosion testing.

2.3. Phase simulation and heat treatment of NiFDSS

Fig. 2 displays the temperature-dependent volume fractions of various phases in NiFDSS, determined using the Thermo-Calc software by using the chemical composition of the powder as the input. The X-axis denotes the temperature range, while the Y-axis shows the equilibrium phase volume fraction. Based on the graph, 950 °C was identified as the optimal heat treatment temperature since both ferritic and austenitic phase fractions are equal at this temperature, creating a duplex structure, considering no deviation from powder composition. Furthermore, undesirable phases such as sigma, chi, and other intermetallics were unstable at this temperature. The heat treatment was carried out in a Nabertherm box muffle furnace under normal atmospheric conditions, with the furnace heated to 950 °C with a heating rate of 10 °C/min and held at this temperature for 1 h. Then, the samples were quenched in water.

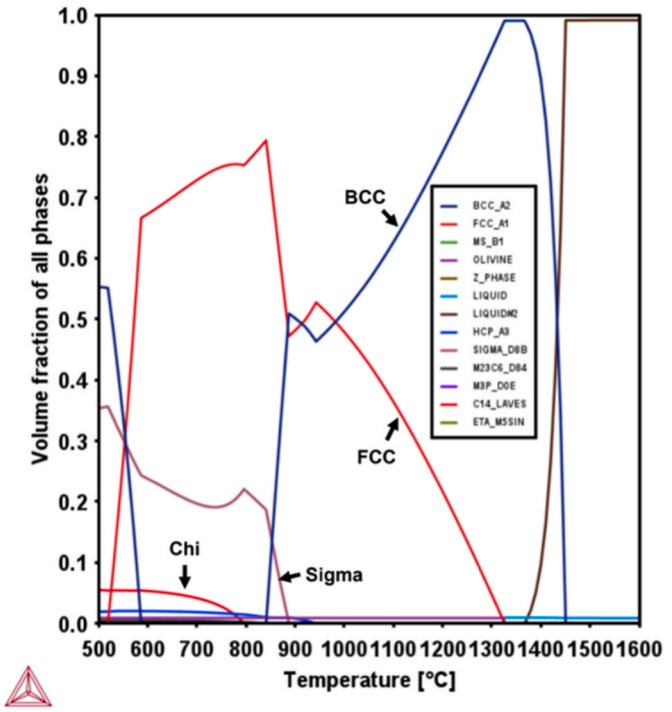

Fig. 2. Phase fractions as a function of temperature in NiFDSS, as calculated using Thermo-Calc.

2.4. Material characterization

For material characterization, as-built 316L, as-built NiFDSS, and heat-treated (HT) NiFDSS samples were initially prepared by grinding with SiC papers, progressing from coarse 80-grit to fine 4000-grit. Subsequent polishing was performed using diamond suspensions with particle sizes of 3 μm, 1 μm, and 0.25 μm to achieve a smooth surface. Finally, the specimens were polished with oxide polishing suspension (OPS) and subjected to nanoindentation tests using a CSM Instruments Nanoindentation Tester. Furthermore, the polished samples were subjected to broad ion-beam milling using Hitachi IM5000 CTC to observe the microstructure. The Sinus method was employed to a maximum indentation depth of 1 μm, with a loading and unloading rate of 7.5 mN/min and a 10-s pause at maximum load. Ten indents were conducted for each material at room temperature, with a 5 μm spacing between indents. The load-displacement data were analyzed using the Oliver & Pharr method to obtain the elastic modulus [28,29]. Vickers microhardness test was conducted using a Falcon 608 hardness tester on the HV1 scale with a 10-s dwell time, with eight measurements for each sample.

XRD analysis was conducted on 316L and NiFDSS powders and on as-built 316L, as-built NiFDSS, and HT NiFDSS samples. The measurements were performed using a Malvern Panalytical Empyrean system with Cu-Kα radiation, collecting diffraction data over a 2θ range of 20°–90°. For EBSD analysis, cross-sectional samples were embedded in conductive resin to ensure proper conductivity and subsequently polished to a mirror-like finish using a 0.02 μm OPS after initial grinding with SiC papers. The analysis was conducted with a Zeiss Crossbeam 540 SEM paired with an EDAX Hikari Plus EBSD detector, using a 20 keV accelerating voltage, 3 nA beam current, and a 15 mm working distance. Scanning was performed with a step size of 300 nm, and the resulting data were used to generate phase maps, inverse pole figures, and misorientation angle distributions. Additionally, with optimized parameters, the surface roughness of the as-built 316L and as-built NiFDSS samples was measured using a Bruker Alicona Infinite Focus G6 confocal microscope. Nitrogen and oxygen contents in as-built 316L and NiFDSS samples were measured by carrier-gas extraction on a LECO TC-500 analyzer in accordance with ASTM E1019 [30].

2.5. Tribocorrosion evaluation

2.5.1. Electrolyte used

Based on previously conducted studies [31,32] and the ASTM D1141-98 standard [33], an artificial seawater solution was prepared to mimic the marine environment conditions by dissolving NaCl to a concentration of 0.6 M in distilled water, with the pH subsequently adjusted to 8.2 using a 0.1 M NaOH solution.

2.5.2. Tribocorrosion setup

For the tribocorrosion testing, as depicted in Fig. 3, a DUCOM POD 4.0 ball-on-disc tribometer was used alongside a three-electrode setup and an IviumSoft Vertex potentiostat. Wear and corrosion rates were measured simultaneously using two monitors. The sample under test was connected as the working electrode (WE), while a platinum wire and Ag/AgCl (3 M KCl) were utilized as the counter electrode (CE) and reference electrode (RE), respectively. Prior to the tribocorrosion test, the samples were ground with 4000-grit SiC paper and polished with diamond suspensions (3 μm, 1 μm, and 0.25 μm) to achieve a mirror-like finish (surface roughness <0.3 μm). The polished samples were then ultrasonicated in a mixture of acetone and ethanol to eliminate any contaminants.

2.5.3. Electrochemical corrosion test in static condition

A corrosion test was conducted under static conditions without counterload or rotation. After a 1 h immersion in artificial seawater to stabilize the passive film, the polarization scan was conducted within a range of −0.8 V to +0.8 V (vs Ag/AgCl), with a scan rate of 0.5 mV/s and a potential step size of 0.1 mV. After completing the test, polarization curves were recorded for as-built 316L, as-built NiFDSS, and HT NiFDSS. The curves were analyzed using a model data analysis tool available in the IviumSoft software package to determine the corrosion rate. The software calculated the corrosion rate (CR) after inputting the exposed surface area, equivalent weight, and density values using the formula [34]:

$$Corrosion\ rate\ (CR\ \ in\ mm\ /\ year) = \frac{3.276 \times I_{corr} \times Atomic\ Mass}{nF \times Density\ of\ sample}$$

The parameter I_{corr} represents the current density over the surface area of the working electrode, n denotes the stoichiometric number of electrons involved in the electrochemical reaction, and F is Faraday's constant, equal to 96,485 C/mol. The exposed surface area to the electrolyte was 25.05 cm^2 for all samples. The equivalent weight was determined using ASTM Designation G: 102-89 [35], resulting in values of 25.59 g for NiFDSS and 25.56 g for 316L. Based on the chemical composition of the materials, the theoretical densities were calculated as 7.90 g/cm^3 for 316L and 7.73 g/cm^3 for NiFDSS. Ultimately, the corrosion rates of all the samples were determined.

2.5.4. Tribocorrosion test

To simulate tribocorrosion conditions via disrupting the passive oxide layer, a 6 mm alumina ball was mounted in a holder and placed in contact with the sample, with a counter load of 60 N applied at the opposite end. The system was rotated at 10 RPM, and the wear track diameter was 6 mm. The low-speed, high-contact-stress configuration was selected to keep the contact in boundary lubrication, thereby maximising wear-corrosion synergy and providing a benchmark for comparing material performance. Before tribocorrosion testing, each sample was immersed for 1 h in the electrolyte to establish a stable electrochemical surface condition. The tribological test was initiated 2 min before the polarization scan and ran for a total of 56 min to align with the 54-min duration of the potentiodynamic test, conducted from −0.8 V to +0.8 V (vs Ag/AgCl) at a scan rate of 0.5 mV/s and a potential

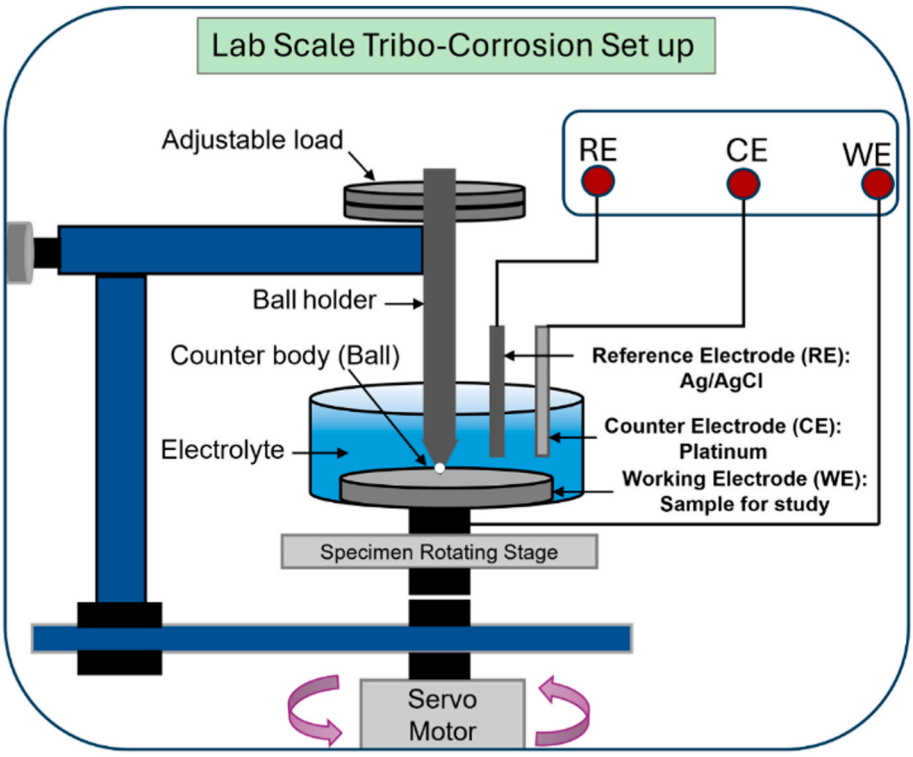

Fig. 3. Schematic depicting a ball-on-disc experimental setup for tribocorrosion used in this study.

step of 0.1 mV. The corrosion rate was computed using IviumSoft software, following the same procedure as the static test. Real-time monitoring of the coefficient of friction (CoF) during tribocorrosion testing was carried out using DUCOM software, which processed data obtained from strain gauges affixed to the load arm. Wear volume was measured by conducting optical profilometry on the wear scars, utilizing the MetaMax software with the Bruker Alicona Infinite Focus G6 system, by integrating the height difference between the scar floor and the adjacent unworn reference plane of the polished surface. SEM and EDS were employed to study the wear tracks after the tribocorrosion testing. The wear rate was calculated using the formulas [36]:

$$Wear\ rate\ \left(mm^2.N^{-1}\right) = \frac{Wear\ volume\ (mm^3)}{Sliding\ distance\ (mm) \times Counter\ load\ (N)}$$

$$Sliding\ distance\ (mm) = 2\pi \times Wear\ track\ radius\ (mm) \times time\ (minutes) \times RPM$$

3. Results and discussions

3.1. Basic characterization and phase analysis

Carrier-gas extraction analysis showed that for as-built NiFDSS, the nitrogen content fell from 0.18 wt% in the powder to 0.15 wt% in the as-built sample, while oxygen level rose from 0.02 to 0.05 wt%. Based on Schaeffler and Delong's equations [37], the chromium equivalent was evaluated using the equation Cr_{eq} = [Cr]+1.4[O]+1.5[Si]+0.5[Nb], and the nickel equivalent using Ni_{eq} = [Ni]+30([C]+[N])+0.5[Mn]. Substituting these values into the equations, in the case of NiFDSS, the changes in chemical composition during PBF-LB/M lowered Ni_{eq} from 9.64 % to 9.40 % and raised Cr_{eq} from 22.89 % to 22.93 %, increasing the Cr_{eq}/Ni_{eq} ratio from 2.37 to 2.44. The resulting Cr_{eq}/Ni_{eq} ratio of 2.44 still exceeded 1.95, indicating that the NiFDSS is expected to exhibit a duplex microstructure with both austenite and ferrite phases [22,38]. For 316L, the nitrogen content decreased from 0.10 to 0.08 wt % and oxygen went from 0.02 to 0.03 wt%, so Cr_{eq}/Ni_{eq} changed to 1.13, which was still below 1.25, confirming a fully austenitic microstructure [39]. In as-built NiFDSS samples, PREN was only marginally reduced, from 30.82 to 30.39, so the alloy still exceeds the 30 threshold for high pitting resistance. For 316L, PREN changed from 24.46 to 24.14.

Fig. 4 depicts the phase composition of the powder particles and the samples examined in this study. For 316L, XRD patterns of both powder and as-built samples showed only austenitic (γ) peaks, attributed to its austenitic-mode solidification pathway (L → L + γ → γ) since $Cr_{eq}/Ni_{eq} < 1.25$. This ensures the stability of the austenitic phase, even under rapid cooling conditions such as gas atomization and PBF-LB/M. In contrast, NiFDSS powders and as-built samples displayed only ferritic (δ) peaks due to their ferritic-mode solidification pathway (L → L + δ → δ → δ + γ → γ), with $Cr_{eq}/Ni_{eq} > 1.95$. High cooling rates during gas atomization and PBF-LB/M (10^5–10^6 K/s) suppressed the δ to γ transformation, resulting in a fully ferritic microstructure [15]. Heat treatment of the as-built NiFDSS sample at 950 °C facilitated the formation of a duplex microstructure by promoting δ to γ transformation, which was subsequently retained upon quenching, as evidenced by XRD peaks corresponding to both ferrite and austenite phases.

SEM cross-sectional imaging normal to the build direction (Fig. 5) showed microstructural features of the specimens. The as-built 316L (Fig. 5 (a)) exhibited semi-circular, overlapping melt-pool boundaries, with fine-subgrains cellular features indicative of rapid solidification. The as-built NiFDSS (Fig. 5 (b)) demonstrated a square-like mosaic macrostructure composed of equiaxed tesserae approximately 60–100 μm wide. Upon heat treatment at 950 °C followed by water quenching, the NiFDSS sample (Fig. 5(c)) displayed continuous crack networks. Closer inspection (Fig. 5 (d)) revealed sigma-phase precipitation across the cracks. These brittle intermetallics promoted local embrittlement, thereby facilitating the initiation and propagation of cracks during quenching.

EBSD imaging in Fig. 6 confirmed the phase composition of the samples. The as-built 316L matrix consisted of 99.9 % austenite, while the as-built NiFDSS was primarily ferritic, with 98.8 % ferrite. Following heat treatment, as shown in Fig. 6 (c), the HT NiFDSS developed a

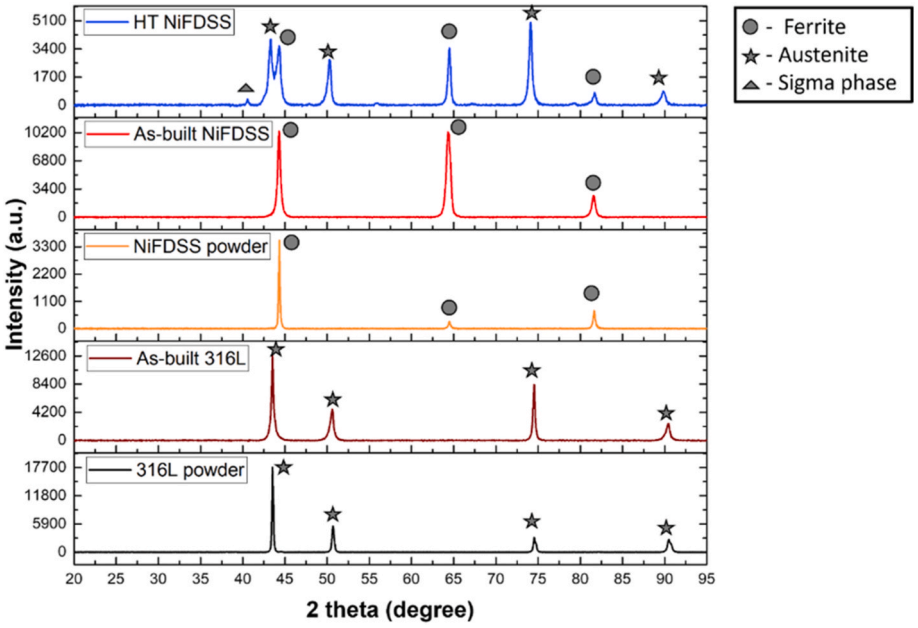

Fig. 4. XRD peaks correspond to the phases present in 316L and NiFDSS powder, as-built 316L, as-built NiFDSS, and HT NiFDSS samples.

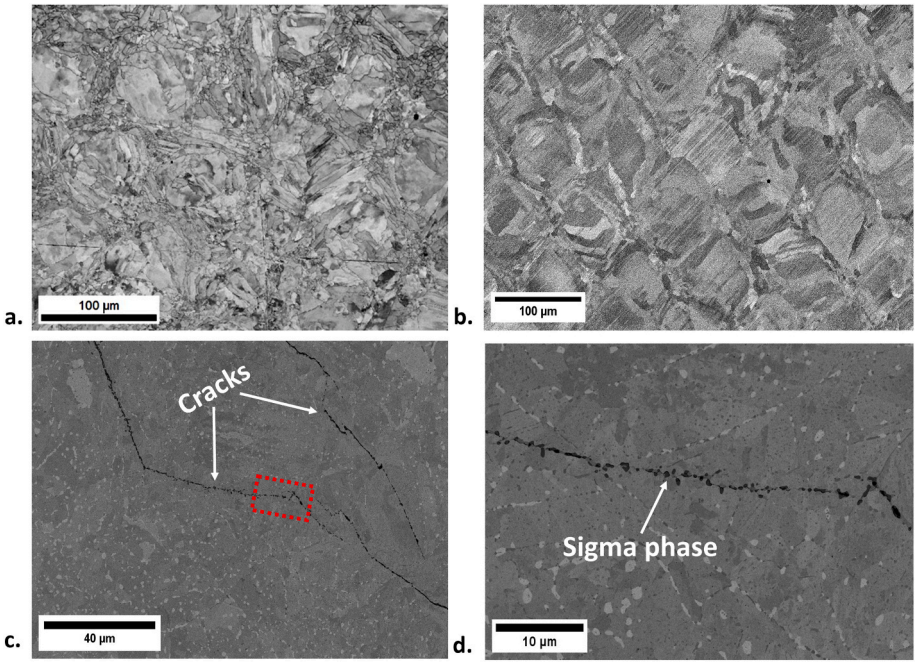

Fig. 5. SEM micrographs of (a) as-built 316L, (b) as-built NiFDSS, (c) HT NiFDSS showing quench cracks (arrows), and (d) magnification of the red dashed box in (c), revealing sigma phase.

duplex microstructure comprising 61.4 % ferrite, 34.8 % austenite, and 3.8 % sigma phase. Compared to the phase fraction showing nearly equal percentages of austenite and ferrite with no precipitates at 950 °C, as shown in Fig. 6 (c), the higher percentage of ferrite in the heat-treated sample resulted from the evaporation of the austenitic stabilizer nitrogen during the PBF-LB/M process, resulting in higher Cr_{eq}/Ni_{eq}, driving the composition deeper into the ferritic domain of the Schaeffler diagram and accounting for the ferrite-rich matrix and sigma-phase precipitation observed after heat treatment [40]. Additionally, although the cooling rates are typically high during water quenching, they may not be rapid enough to completely prevent the sigma phase formation. As a result, there was sufficient time for sigma phase precipitation, particularly within the austenitic phase, evidenced by the dark black dots present in the austenite region, shown in Fig. 6 (c).

Fig. 7 illustrates the inverse pole figures maps and misorientation angle distributions obtained perpendicular to the build direction. As-built 316L and NiFDSS exhibited a higher proportion of high-angle grain boundaries (HAGBs) compared to low-angle grain boundaries (LAGBs), which primarily resulted from the directional solidification of molten metal during the process [41]. For the HT NiFDSS, the misorientation distribution was dominated by LAGBs, which could be attributed to dynamic recovery and subgrain formation during heating to 950 °C, with rapid water quenching preserving these substructures by suppressing recrystallization [42,43].

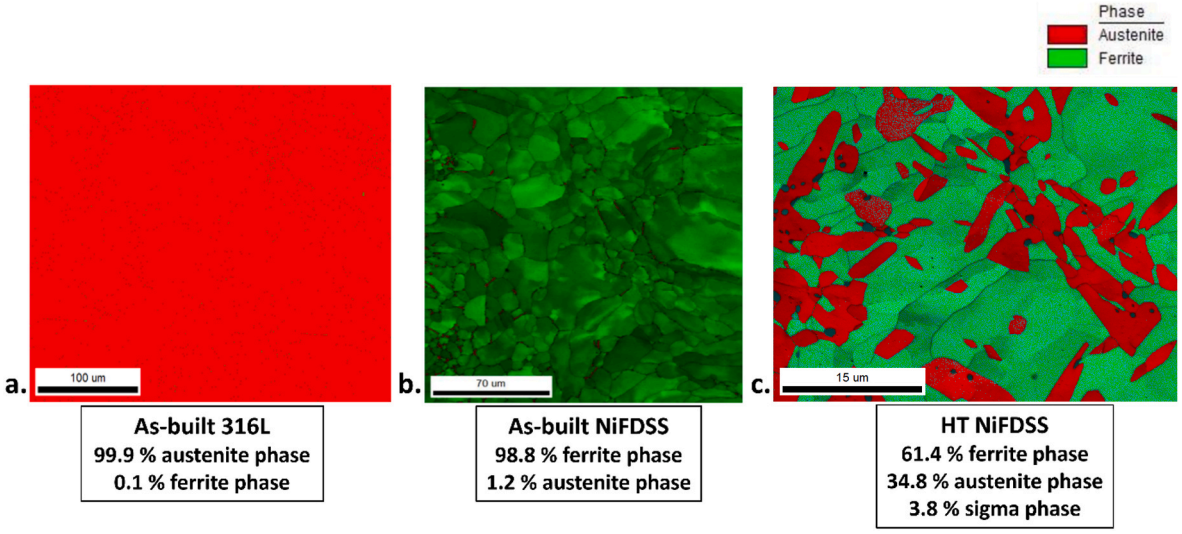

Fig. 6. EBSD phase mapping of the specimens, in which red corresponds to the austenite phase, green corresponds to the ferritic phase, and small dark black dots correspond to the sigma phase.

Fig. 8 shows the load-displacement curves from nanoindentation tests, while the full dataset of 30 curves (10 measurements per material) is included in the supplementary material (Fig. A5). NiFDSS exhibited the steepest slope during the loading phase, indicating the highest stiffness and hardness among the materials. HT NiFDSS showed intermediate stiffness and elastic recovery, reflecting the effects of heat treatment on its microstructure. 316L had the lowest slope and elastic recovery, consistent with its lower mechanical strength and higher ductility. The elastic modulus values obtained from nanoindentation tests are shown in Table 2. The higher variation observed in HT NiFDSS was attributed to its duplex microstructure, where the indentation might target either ferritic or austenitic regions, leading to localized variations in mechanical properties.

As shown in Table 2, as-built NiFDSS exhibits maximum hardness owing to its fully ferritic structure. The ferrite phase is harder than the austenite phase [44]. Since the heat-treated NiFDSS contained both phases, its hardness fell between the as-built NiFDSS and as-built 316L. The measured surface roughness (S_a) was 11.26 μm for as-built 316L and 8.68 μm for as-built NiFDSS. As-built 316L samples displayed more pronounced peaks and valleys, indicating more surface irregularities than NiFDSS (Fig. A6). The greater roughness in as-built 316L could be attributed to the larger particle size, as particle size distribution influences surface finish, with coarser particles resulting in a rougher surface [45].

3.2. Corrosion rate under static conditions

The corrosion behavior of 316L, NiFDSS, and HT NiFDSS was studied through polarization curves, as shown in Fig. 9. Among the samples in Table 3, the as-built 316L exhibited the maximum open circuit potential (OCP), attributed to its higher chromium content in alloy composition, facilitating the formation of a stable and protective passive film. However, its passive film displayed higher susceptibility to breakdown in the chloride environment, as reflected by the highest I_{corr}, which resulted in a maximum CR. In comparison, as-built NiFDSS, with a higher PREN (30.39) than 316L (24.14), demonstrated better resistance to corrosion despite its lower chromium content and OCP. Molybdenum and nitrogen are well known to strengthen the passive film and improve pitting resistance, often working synergistically [46]. Nitrogen enhances re-passivation by consuming acidic species in pit solutions, buffering the local pH, and inhibiting pit growth, while molybdenum enriches and stabilizes the passive layer by forming protective molybdenum-oxides [47]. Thus, the higher PREN, attributed to the increased molybdenum and nitrogen content in NiFDSS, enhanced its resistance to chloride-induced corrosion in seawater [48], resulting in a reduced I_{corr} and CR.

Due to its duplex microstructure, HT NiFDSS had the lowest I_{corr} (0.646 μA/cm^2) and CR (0.007 mm/year). The synergistic interaction between ferritic and austenitic phases stabilized the passive film, thereby improving corrosion resistance [49]. Chromium and molybdenum partitioned preferentially into the ferritic phase, while nitrogen and maganese enriched in the austenitic phase [50]. This balanced distribution of alloying elements gave each phase a distinct role in corrosion protection: the chromium/molybdenum-rich ferrite promoted rapid formation of a stable passive layer with high pitting resistance, whereas the austenite improved re-passivation kinetics and maintained the overall stability of the film.

3.3. Tribocorrosion analysis

3.3.1. Corrosion rate during tribocorrosion

The corrosion behavior of 316L, NiFDSS, and HT NiFDSS under tribocorrosion, where the passive film was disrupted, was evaluated, as shown in Fig. 10. Compared to static conditions, mechanical wear and electrochemical reactions under tribocorrosion resulted in noticeable changes in OCP and CR. Under tribocorrosion, 316L exhibited the lowest OCP (Table 4), transitioning from the noblest material in static conditions to the most reactive, suggesting that the passive film in 316L was highly susceptible to mechanical damage and unable to repassivate effectively. Conversely, NiFDSS and HT NiFDSS demonstrated higher OCP values, indicating superior repassivation during wear.

The CR analysis revealed that HT NiFDSS retained the lowest CR (0.010 mm/year), although it increased by 42.9 % compared to static conditions (0.007 mm/year). NiFDSS showed a CR of 0.019 mm/year, a 35.7 % rise from its static CR (0.014 mm/year). In contrast, 316L experienced the smallest increase (5.3 %), with its CR changing only marginally from 0.019 mm/year (static) to 0.020 mm/year (tribocorrosion). The greater percentage increase in CR for NiFDSS and HT NiFDSS compared to 316L was attributed to more areas being exposed to corrosion due to higher wear during tribocorrosion 43,51, which will be analyzed in the next section. In essence, wear-induced depassivation played a dominant role: the as-built and HT NiFDSS samples, despite having superior inherent corrosion resistance, suffered extensive passive film removal from their higher wear rates. The continuous stripping of the film forced these alloys to constantly repassivate, elevating their corrosion currents. By contrast, lower wear of 316L meant less fresh

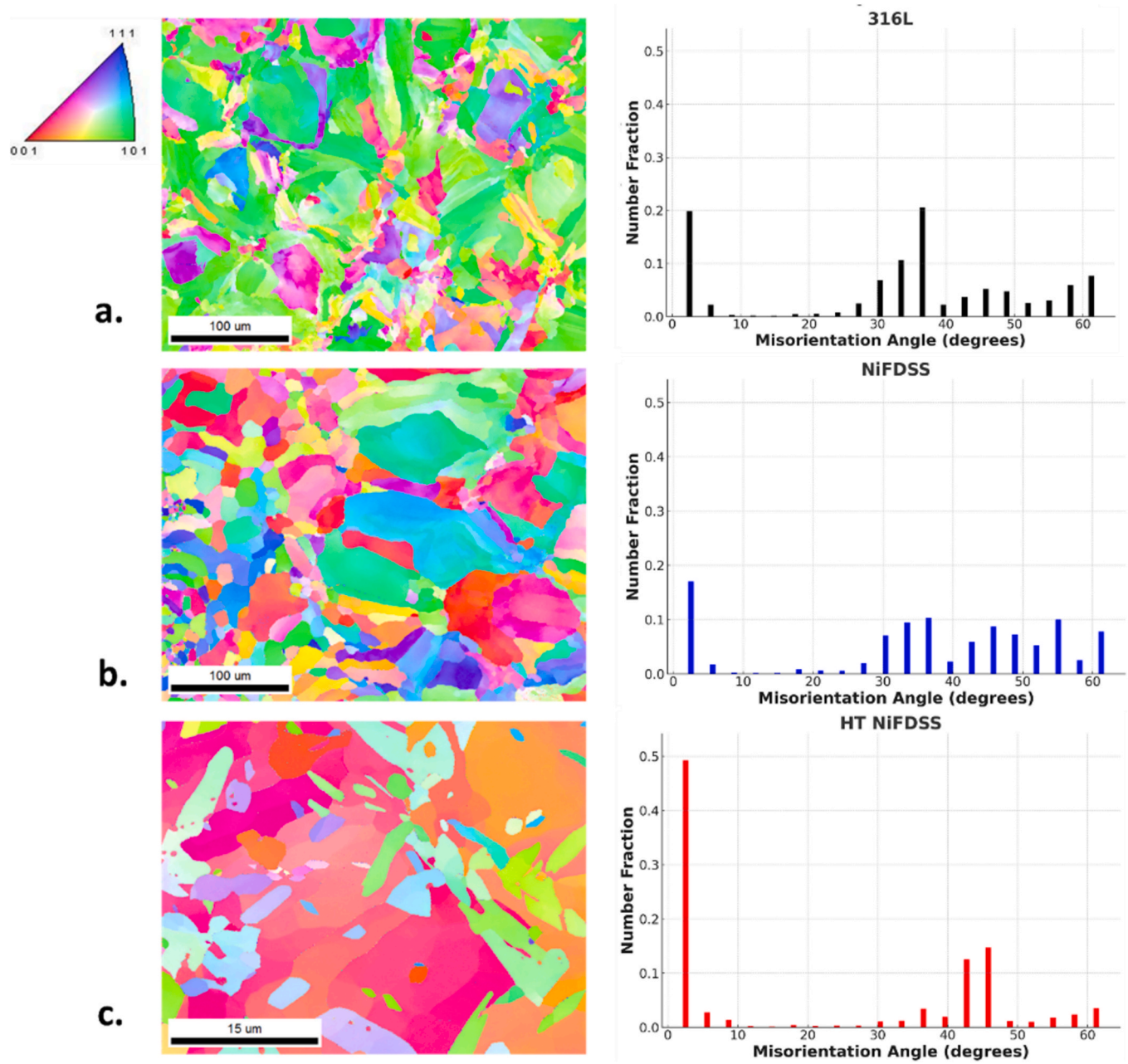

Fig. 7. Inverse Pole Figures maps and misorientation angle distributions for (a) 316L, (b) NiFDSS, and (c) HT NiFDSS.

metal exposure, so it experienced only a slight increase in corrosion rate even though its passive film was less robust.

HT NiFDSS maintained the lowest CR due to its efficient repassivation dynamics, where its duplex microstructure likely promoted rapid film regeneration on freshly exposed surfaces, offsetting the impact of higher wear. Also, the presence of sigma-phase precipitates in HT NiFDSS could have introduced localized galvanic effects that further influenced its tribocorrosion behavior. The sigma-phase is relatively cathodic and remains protected, while the surrounding matrix becomes depleted in chromium/molybdenum and thus anodically dissolves more readily, reducing the overall corrosion resistance of DSS [52]. Despite this, in the present experiments the dominant factor for HT NiFDSS was still its rapid re-passivation ability conferred by the duplex microstructure, which kept its overall corrosion rate the lowest among the tested materials.

3.3.2. *Wear behavior and analysis of the wear track*

The relationship between the coefficient of friction (CoF) and the sliding time of 316L, NiFDSS, and HT NiFDSS is illustrated in Fig. 11 (a). The average CoF for 316L, NiFDSS, and HT NiFDSS was found to be 0.35 $\pm$ 0.02, 0.19 $\pm$ 0.01, and 0.32 $\pm$ 0.02, respectively. As-built NiFDSS had the lowest CoF, which could be due to its highest hardness (399 $\pm$ 25 HV), which was approximately 65 % higher than 316L (242 $\pm$ 8 HV) and 32 % higher than HT NiFDSS (303 $\pm$ 21 HV). In the initial phase (0–2 min), before the application of cathodic polarization, frictional behavior was primarily governed by mechanical interactions. During this period, the coefficients of friction for 316L, NiFDSS, and HT NiFDSS were recorded as 0.40, 0.20, and 0.28, respectively. NiFDSS, with a fully ferritic microstructure and the highest hardness, had nearly 40 % higher CoF than HT NiFDSS. In contrast, 316L, with a fully austenitic microstructure with the lowest hardness, showed the highest CoF due to greater surface adhesion and plastic deformation. Meanwhile, HT NiFDSS with its duplex microstructure showed CoF between 316L and

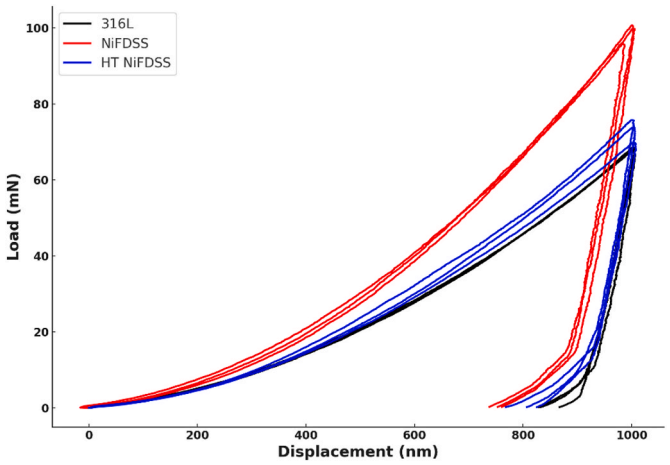

Fig. 8. Load-displacement curves for 316L, NiFDSS, and HT NiFDSS obtained through nanoindentation testing.

Table 2
Elastic modulus and Vickers microhardness calculated for 316L, NiFDSS, and HT NiFDSS.

	316L	NiFDSS	HT NiFDSS
Elastic modulus (GPa)	151 ± 12	236 ± 15	195 ± 19
Vickers microhardness (HV)	242 ± 8	399 ± 25	303 ± 21

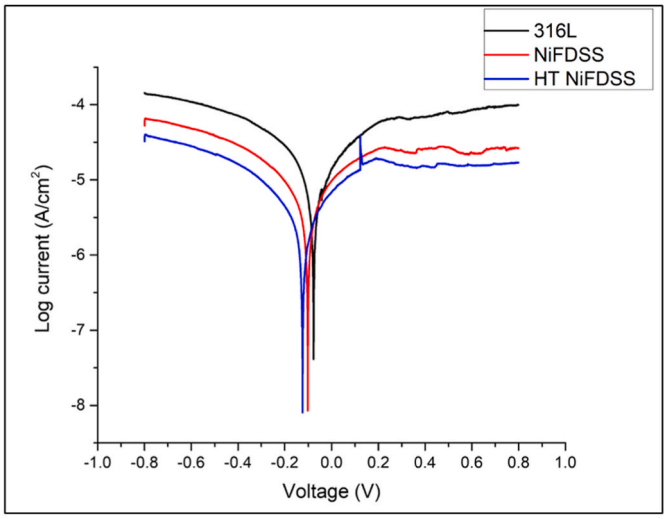

Fig. 9. Potentiodynamic polarization curves for 316L, NiFDSS, and HT NiFDSS in a simulated seawater environment (0.6 M NaCl, pH 8.2) under static conditions.

Table 3
Analysis of the data using IviumSoft software, providing comparisons of open circuit potential (OCP) in volts (mV), corrosion current density (I_{corr}) in Amperes (**μ**A)/cm^2, and corrosion rate (CR) in mm/year.

	316L	NiFDSS	HT NiFDSS
OCP (mV)	−75 ± 8	−102 ± 13	−123 ± 9
I_{corr} (μA/cm^2)	1.78 ± 0.11	1.30 ± 0.19	0.65 ± 0.16
CR (mm/year)	0.019 ± 0.001	0.014 ± 0.002	0.007 ± 0.002

NiFDSS.

During the cathodic polarization period (2–29 min), CoF stabilized for NiFDSS and HT NiFDSS due to improved electrochemical stability

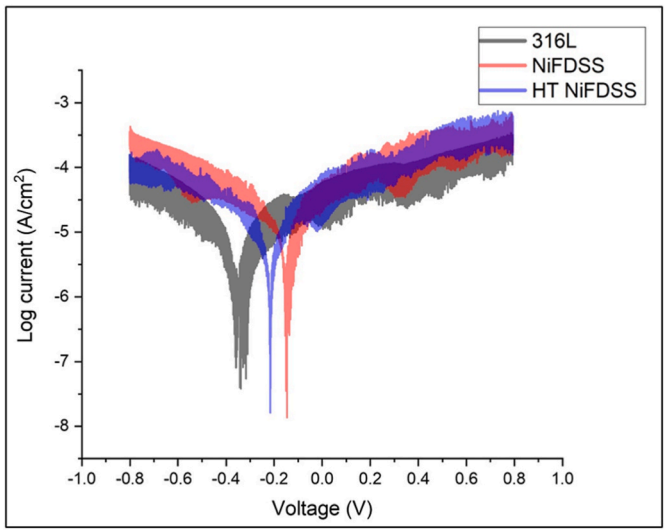

Fig. 10. Potentiodynamic polarization curves of 316L, NiFDSS, and HT NiFDSS in an artificial seawater environment (0.6 M NaCl) with pH 8.2 during wear testing against an alumina ball.

Table 4
Data extracted from analyzing the curves using IviumSoft software, comparing open circuit potential (OCP) in volts (mV), corrosion current density (I_{corr}) in amperes (**μ**A)/cm^2, and corrosion rate (CR) in mm/year.

	316L	NiFDSS	HT NiFDSS
OCP (mV)	−334 ± 35	−145 ± 20	−212 ± 17
I_{corr} (μA/cm^2)	1.90 ± 0.38	1.72 ± 0.14	0.90 ± 0.23
CR (mm/year)	0.020 ± 0.006	0.019 ± 0.002	0.010 ± 0.003

and reduced corrosion-induced wear. However, 316L exhibited three notable transitions in CoF. A sharp decrease in CoF around ~7 min and continued to be stable till 20 min of sliding was likely related to a smoother wear track developing from wear debris compaction or local surface smoothing. The subsequent rise in CoF was observed for 20–26 min, and CoF reached 0.40, which was linked to partial surface disruption or changes in wear track morphology. SEM images (Fig. 13 (a–d)) confirmed fewer cracks and surface fragments for 316L compared to NiFDSS (Fig. 13(e–h)) and HT NiFDSS (Fig. 13(i–l)), reflecting lower surface damage despite CoF fluctuations. The decrease at ~40 min might result from further compaction or rearrangement of wear debris on the wear track during tribocorrosion.

The wear volume of the samples, obtained from optical profilometry of wear scars, as illustrated in Fig. 12, was measured to be 0.020 ± 0.003 mm^3 for as-built 316L, 0.025 ± 0.004 mm^3 for as-built NiFDSS, and 0.030 ± 0.007 mm^3 for HT NiFDSS. The pseudo colors depicted the depth of the worn scar, with magenta highlighting the greater depth of wear. The measured wear volume, obtained from optical profilometry, was used to calculate the wear rate.

Fig. 11 (b) presents the average wear rate of NiFDSS under applied loads of 60 N and a sliding speed of 10 RPM. The average wear rate of 316L, NiFDSS, and HT NiFDSS was found to be 3.19 ± 0.03 × 10^{-8} mm^3/N.m, 3.95 ± 0.05 × 10^{-8} mm^3/N.m, and 4.74 ± 0.08 × 10^{-8} mm^3/N.m, respectively. Sample 316L demonstrated the lowest wear rate due to its ductile austenitic structure, which resisted material removal by undergoing substantial work hardening during sliding contact, meaning the surface layer became progressively stronger and more wear-resistant as it deformed.

Although NiFDSS exhibited an elastic modulus (236 ± 15 GPa) approximately 57 % higher than that of 316L, it demonstrated a nearly 24 % higher wear rate than 316L. The counter-intuitive increase was attributed to surface-connected lack-of-fusion pores (Fig. A7), which

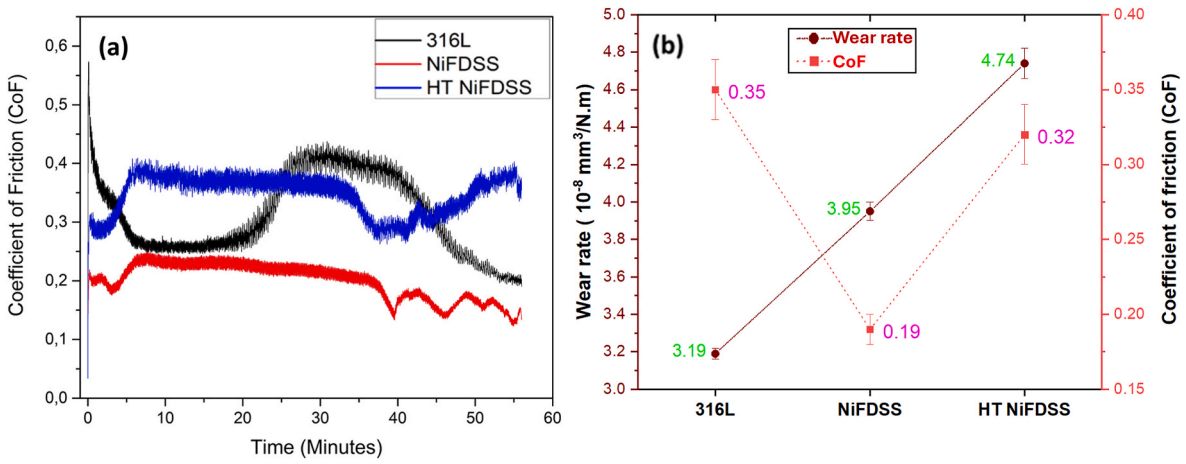

Fig. 11. (a) Plots of coefficient of friction (CoF) of PBF-LB/M of 316L, NiFDSS, and HT NiFDSS vs. the sliding time and (b) average wear rate ($\times 10^{-8}$ mm^3/Nm) and CoF of 316L, NiFDSS, and HT NiFDSS.

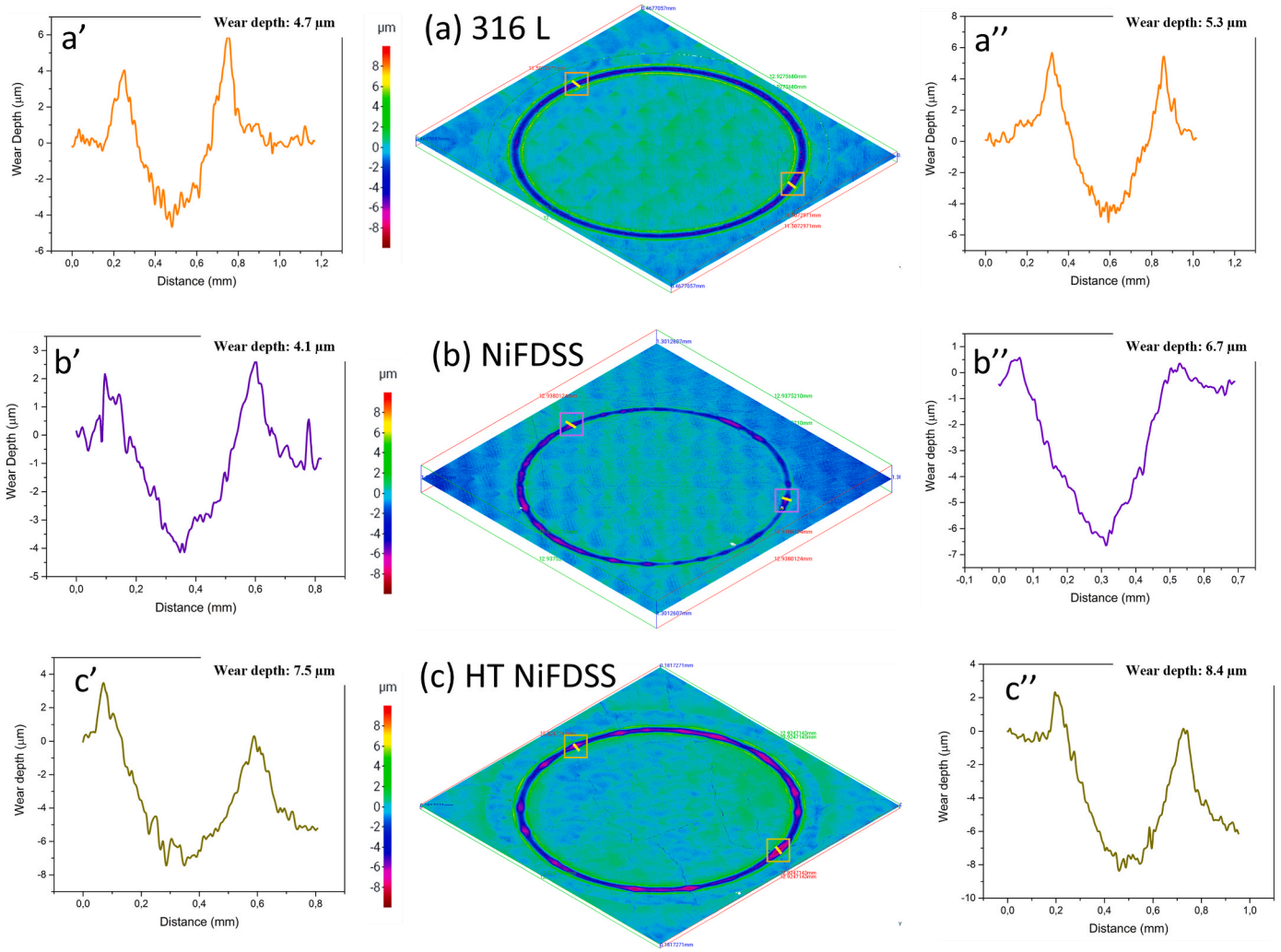

Fig. 12. Optical profilometry images of wear scars and corresponding depth profiles for (a) as-built 316L, (b) as-built NiFDSS, and (c) HT NiFDSS. Pseudocolor maps represent the depth of the wear scars, while the depth profiles (a', a'', b', b'', c', and c'') illustrate the variation in wear depth across the scar regions.

intensified local contact stresses, expanding during tribocorrosion and contributing to higher material removal [53]. The greater stiffness and limited ductility in as-built NiFDSS made it less able to redistribute stresses at the contact interface. It could not elastically blunt asperities as effectively as 316L, so defects like pores became focal points for stress and crack initiation. Consequently, even though the as-built NiFDSS was harder, its wear progressed via brittle fracture and particle spallation rather than smooth plastic wear, elevating its overall wear rate. Also,

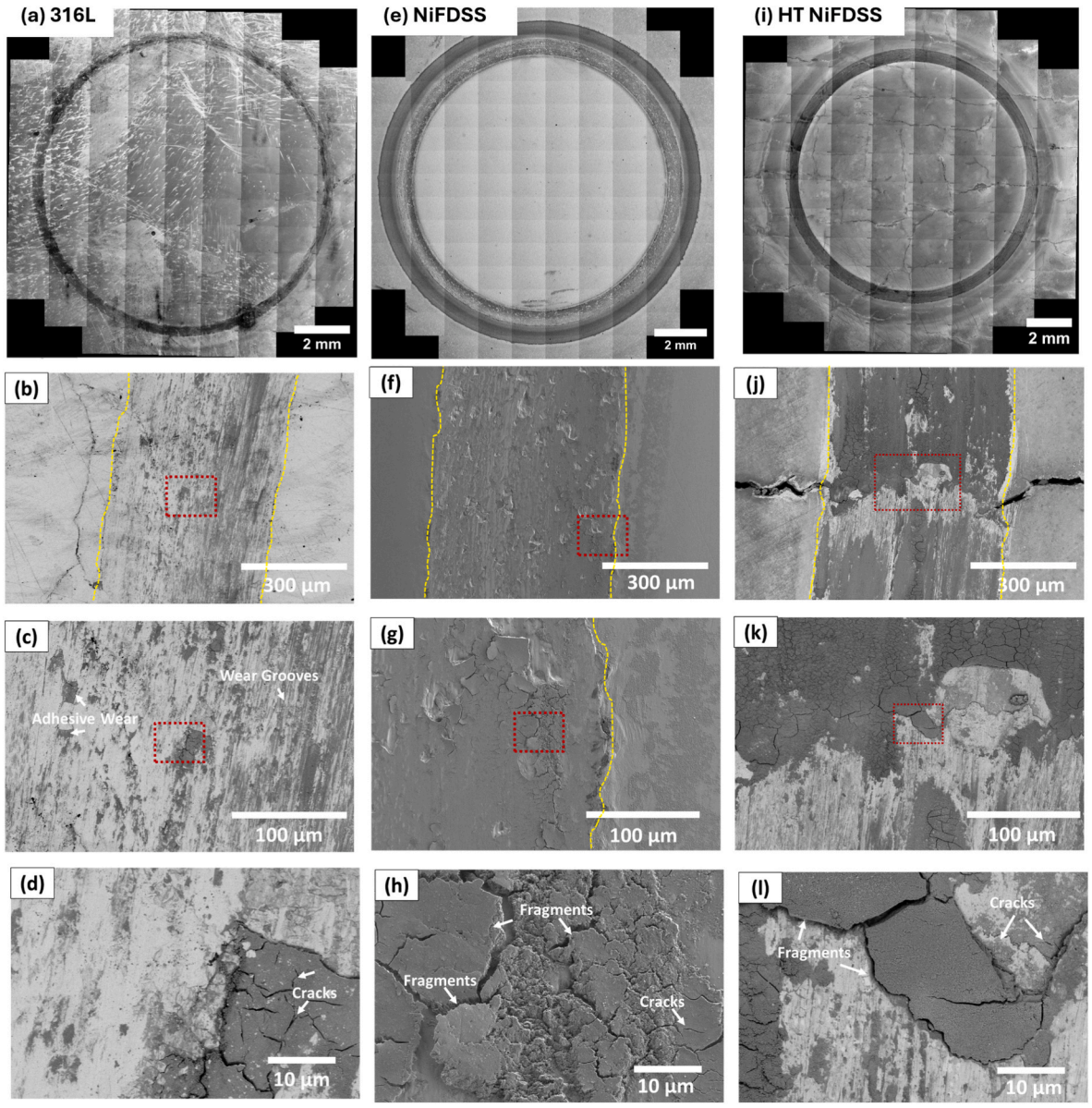

Fig. 13. Scanning electron micrographs of wear scars for (a–d) as-built 316L, (e–h) as-built NiFDSS, and (i–l) HT NiFDSS under various magnifications.

as-built NiFDSS solidified as body-centred-cubic (BCC) ferrite, which had limited independent slip systems. Under sliding contact, it, therefore, accommodated stress by cleavage on {100} planes and by low-ductility delamination [54]. In contrast, 316 L had a face-centred-cubic (FCC) austenitic matrix that offered multiple {111} slip systems, allowing contact stresses to be dissipated through planar slip, micro-ploughing, and strain hardening [55]. Thus, the as-built NiFDSS matrix experienced higher material loss than the 316L.

Although the heat treatment produced the desired duplex microstructure that typically provides a combination of high strength and good toughness, any expected improvement in wear resistance was negated by the formation of brittle sigma-phase precipitates. So, HT NiFDSS, despite its superior static corrosion resistance, showed the highest wear rate. As shown in Fig. 5(c and d), HT NiFDSS exhibited prominent quench-induced intergranular cracking, with SEM analysis revealing a continuous precipitation of sigma-phase along grain boundaries. The presence of this brittle intermetallic significantly reduced grain-boundary cohesion, facilitating crack initiation and propagation during rapid cooling. Under tribocorrosion conditions, selective corrosion attack along sigma-embrittled boundaries accelerated grain-boundary damage and worked in tandem with mechanical cracking to aggravate wear in HT NiFDSS, resulting in expansion of pre-existing quench cracks and accelerating surface fragmentation and wear. Additionally, brittle debris originating from sigma-phase spallation initially increased friction through abrasive ploughing but subsequently, upon comminution, formed fine third-body particles that partially reduced friction via a rolling mechanism, in line with classical third-body tribological theory [56]. The hard sigma-derived debris gouged the surface, a transient ploughing effect noted in prior studies of sigma-phase-containing duplex steels [57], which explained the temporary friction increase. Even though these fragments eventually pulverized and behaved like rolling third bodies, their initial abrasive action significantly contributed to material removal in HT NiFDSS. The continuous generation, fracture, and removal of these sigma-rich debris particles thus substantially increased material loss and surface degradation, leading to the highest observed wear rate for HT NiFDSS.

For 316L, the average wear depth was relatively consistent, with 4.7 ± 0.5 µm on the left side (Fig. 12 a`) and 5.3 ± 0.3 µm on the right side (Fig. 12 a") of the wear track. In case of as-built NiFDSS, the wear depth increased to 6.7 ± 0.4 µm on the right side (Fig. 12 b") of the wear track

as compared to 4.1 ± 0.2 μm on the left side (Fig. 12 b'), primarily due to the uneven distribution of lack-of-fusion pores. These pores created localized weak points that led to more pronounced wear in those regions, visible as darker magenta spots. After heat treatment, sigma phase precipitation exacerbated cracks and defects, resulting in an even greater wear depth of 7.5 ± 0.5 μm on the left (Fig. 12 c') and 8.4 ± 0.9 μm on the right side (Fig. 12 c") of the wear track in HT NiFDSS samples. The increased wear depths observed in the as-built NiFDSS and HT NiFDSS correlated with their higher wear rates than 316L. So, lack of internal defects in 316L allowed a uniformly shallow wear track, whereas inherent porosity in NiFDSS created weak spots that suffered deeper gouging. Once NiFDSS was heat-treated, the proliferation of sigma-embrittled boundaries meant that almost the entire surface behaved like a collection of weak zones, yielding a consistently deeper and rougher wear scar across the track.

The SEM micrographs in Fig. 13 demonstrate the wear mechanisms for 316L, NiFDSS, and HT NiFDSS. For 316L (Fig. 13 (a)), the unworn regions showed a fully dense surface, while the wear tracks revealed smooth grooves with adhesive wear and fragmented oxide debris (Fig. 13(b–d)). This confirmed the transient formation and removal of

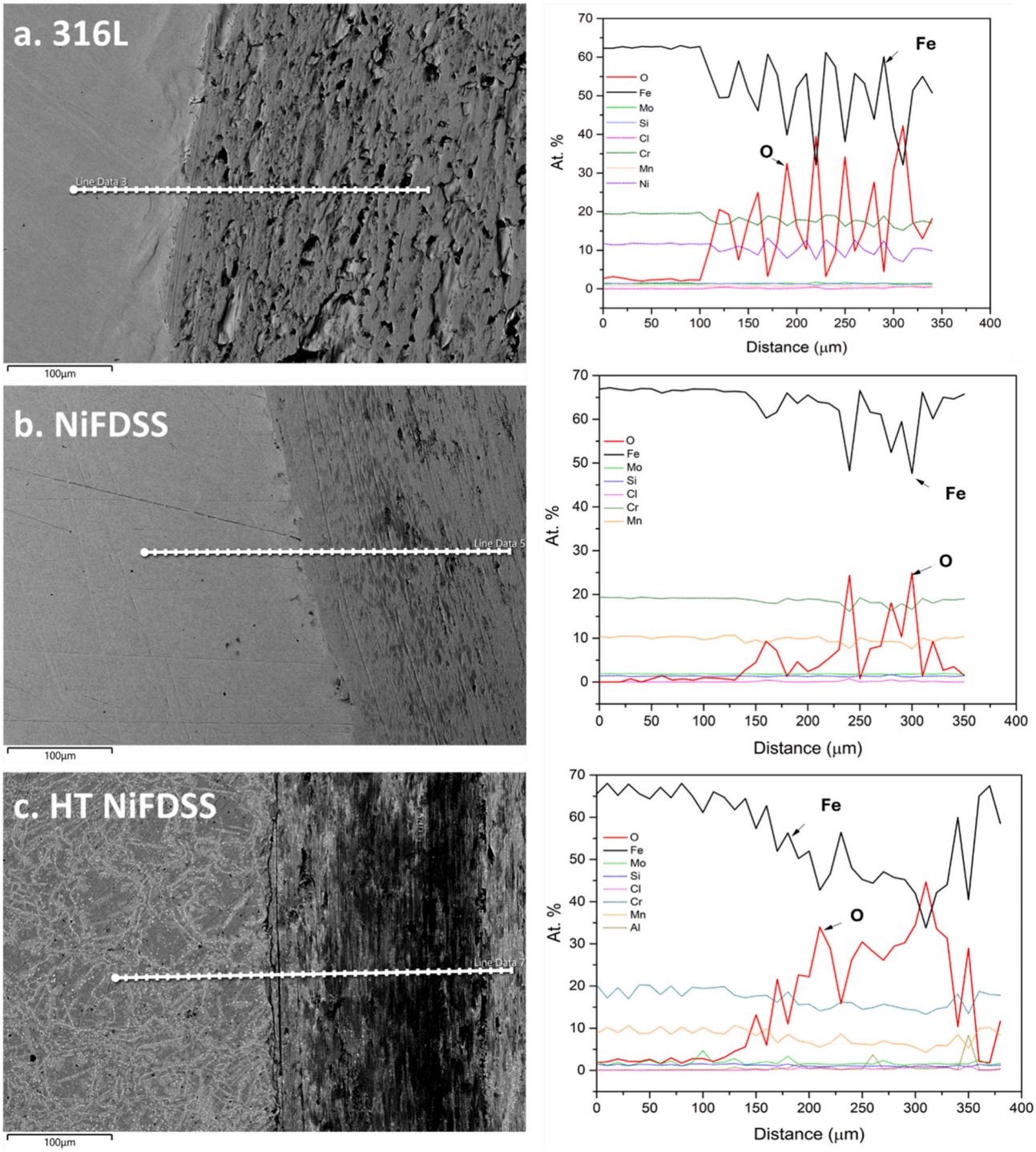

Fig. 14. BSE micrographs and atomic percentage (At. %) profiles of key elements (Fe, Cr, Mn, O, Ni) across the non-wear-to-wear regions for (a) 316L, (b) NiFDSS, and (c) HT NiFDSS.

protective oxide layers, correlating with CoF fluctuations and low wear rates. Such a wear pattern indicated that material in 316L was removed mainly by microscale adhesion and shearing rather than by brittle fracture. NiFDSS (Fig. 13 (e)) had rougher wear tracks with prominent cracks and material fragmentation, reflecting abrasive wear mechanisms (Fig. 13(f–h)). Lack-of-fusion pores were evident in the unworn regions, which likely expanded during tribocorrosion, contributing to material removal and intermediate wear rate ($3.95 \pm 0.05 \times 10^{-8}$ mm^3/N.m).

Also, the wear track was more severe, and steep grooves (Fig. 13 (g)) were observed in the case of as-built NiFDSS compared to 316L. The presence of sharp grooves and fragmented debris in as-built NiFDSS indicated that hard asperities or third-body particles were ploughing the surface, consistent with abrasive wear. Because the ferritic matrix of as-built NiFDSS was unable to deform plastically, these grooves were accompanied by micro-cracks at their edges. Moreover, when sub-surface pores were intersected by the wear process, they opened up and caused chunks of material to break free, further roughening the wear scar.

HT NiFDSS (Fig. 13 (i)) displayed severe cracking, fragmentation, and interconnected fracture networks on the wear track (Fig. 13(j–l)). The cracks (Fig. 13 (j)) acted as stress concentrators, exacerbating crack propagation and material loss. The micro-cracks near abrasive grooves caused substantial fragmentation and delamination (Fig. 13 (l)), which explained its poor wear resistance. This indicated a predominantly brittle failure mode in HT NiFDSS: rather than smoothing out under the load, the surface was breaking apart along the sigma-embrittled grain boundaries. Each crack readily propagated (sometimes assisted by localized corrosion at the crack tip), causing entire pieces of the material to delaminate. This delamination-wear mechanism accounted for the roughest, most damaged wear surface observed in HT NiFDSS.

Fig. 14 shows the SEM images and atomic percentage profiles across the wear and non-wear regions for 316L, NiFDSS, and HT NiFDSS, obtained through an EDS line scan. One prevalent form of wear in these materials was tribo-oxidation, where the heat generated by friction promoted the growth and subsequent detachment of oxide films, influencing the wear dynamics significantly [58]. In 316L (Fig. 14 (a)), Fe and O wt.% variations suggested intermittent oxide formation and removal, consistent with wear debris on the surface. The fragmented metallic debris observed in the wear track aligned with adhesive wear, where material transfer and detachment contributed to localized oxidation.

For NiFDSS (Fig. 14 (b)), a comparatively lower increase in O wt.% indicated reduced tribo-oxidation, supporting the earlier observation that its passive film remained more stable during wear. The smaller oxygen uptake for NiFDSS was indicative of a more resilient passive film during sliding due to its higher PREN, in comparison with 316L, which showed higher oscillating oxygen levels and more oxidation along the wear track. HT NiFDSS (Fig. 14 (c)) exhibited the most pronounced fluctuations in Fe and O, with dark regions in BSE imaging confirming higher oxidation. The high O concentration suggested that tribo-oxidation was dominant in material degradation, with Fe depletion in these regions indicating progressive oxide layer formation and subsequent removal. This supported the previously observed severe wear morphology, where cracking and delamination drove material loss, making HT NiFDSS the most susceptible to wear under tribocorrosion.

The EDS mapping data, presented in Fig. A8 (316L), Fig. A9 (NiFDSS), and Fig. A10 (HT NiFDSS), highlighted elemental variations across the wear, transition, and non-wear regions. Consistent with the line-scan data, the wear regions had elevated oxygen content and fluctuations in Fe wt.%, indicative of oxide formation and material removal during wear. Chlorine was detected in the wear region for all three samples, reflecting that the passive oxide film breakdown facilitated localized chemical interaction with chloride ions from the seawater electrolyte.

The discussion regarding the wear mechanisms described above has been summarized in Fig. 15. The 316L sample (Fig. 15 (a)) showcased more fluctuations in the CoF but maintained a relatively smooth worn scar with a wear depth of 4.7 ± 0.5 μm. It also showed minimal crack formation and reduced debris fragmentation, which aligned with its lowest recorded wear rate of $3.19 \pm 0.03 \times 10^{-8}$ mm^3/N.m. In contrast, the NiFDSS sample (Fig. 15 (b)) demonstrated a moderate wear rate of $3.95 \pm 0.05 \times 10^{-8}$ mm^3/N·m. The presence of lack-of-fusion pores during the printing process contributed to crack development and severe damage during sliding, leading to a rough and deep worn scar with a wear depth of 6.7 ± 0.4 μm. Meanwhile, HT NiFDSS (Fig. 15 (c)) had extensive cracking and fragmentation due to sigma phase precipitation, leading to localized brittle failure despite its relatively stable and low CoF. As a result, HT NiFDSS presented the roughest and deepest worn surface, with a wear rate of $4.74 \pm 0.08 \times 10^{-8}$ mm^3/N·m and a wear depth of 8.4 ± 0.9 μm.

Overall, these findings illustrate a clear trade-off between wear and corrosion performance: the ductile austenitic-phase 316L sustained

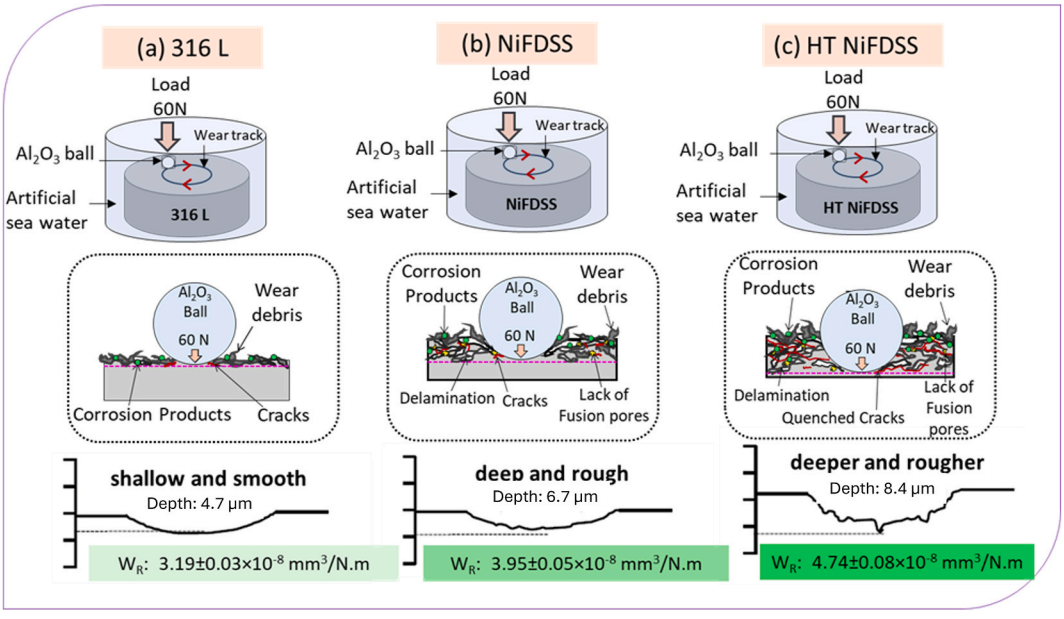

Fig. 15. Schematic of the wear mechanism of (a) 316 L, (b) NiFDSS, and (c) HT NiFDSS in artificial seawater (conditions: normal load: 60 N, against Al_2O_3 ball).

sliding contact with minimal material loss due to plastic deformation and work-hardening, but showed poor repassivation, more oxidation on wear track and higher corrosion rate whereas the NiFDSS variants achieved superior corrosion resistance yet suffered greater wear due to their microstructural brittleness and defects. Improving the tribocorrosion behavior of NiFDSS will require mitigating its lack-of-fusion porosity and preventing sigma-phase embrittlement during heat treatment so that the alloy can retain its corrosion advantages without incurring excessive wear.

4. Conclusions

This study assessed the microstructural, mechanical, corrosion, and wear characteristics of PBF-LB/M fabricated NiFDSS compared to 316L stainless steel in as-built and heat-treated conditions for marine environments. Key findings include:

- Optimized PBF-LB/M parameters manufactured NiFDSS with a 98.83 % relative density. As-built samples had a ferritic microstructure that transformed into a duplex phase after solutionizing at 950 °C and quenching.
- As-built NiFDSS exhibited a lower corrosion rate (0.014 mm/year) compared to 316L (0.019 mm/year), with HT NiFDSS showing the lowest rate (0.007 mm/year), indicating superior passive film stability.
- Tribocorrosion tests revealed that 316L had the lowest wear volume but the highest corrosion rate due to passive film breakdown. As-built and HT NiFDSS displayed higher wear volumes but better corrosion resistance, suggesting more effective repassivation.
- Wear rate analysis showed that HT NiFDSS had the highest wear rate due to quench-induced cracks formed due to sigma phase precipitation that increased material removal, while 316L had the lowest. As-built NiFDSS had the lowest CoF due to its greater hardness, with HT NiFDSS showing an intermediate CoF.
- SEM-EDS analysis identified that 316L underwent adhesive wear with oxide debris formation, as-built NiFDSS showed abrasive wear with localized cracking, and HT NiFDSS experienced significant material loss from quench-induced crack propagation.
- Sigma phase precipitation in HT NiFDSS, due to vaporization-induced elemental compositional shifts that invalidated ThermoCalc predictions, suggests that heat treatment at 1050 °C or above, followed by rapid quenching, is required to dissolve intermetallics and enhance wear performance fully.

CRediT authorship contribution statement

Abhinav Anand: Conceptualization, Methodology, Investigation, Formal analysis, Writing – original draft. **Chinmayee Nayak:** Data curation, Formal analysis, Writing – original draft. **Ermei Mäkilä:** Software, Investigation, Data curation, Writing – review & editing. **Zaiqing Que:** Investigation, Writing – review & editing, Resources, Funding acquisition. **Heidi Piili:** Conceptualization, Supervision. **Sneha Goel:** Conceptualization, Writing – review & editing. **Antti Salminen:** Resources, Funding acquisition. **Ashish Ganvir:** Writing – review & editing, Supervision, Resources, Funding acquisition, Project administration.

Declaration of competing interest

The authors declare that they have no known competing financial interests or personal relationships that could have appeared to influence the work reported in this paper.

Acknowledgments

We appreciate the feedback and suggestions from Vahid Hosseini on performing heat treatment and ThermoCalc simulations. We sincerely thank Aki Piiroinen for his invaluable assistance in procuring the densimeter and performing various laboratory activities. We also thank Frej Björndahl for conducting the particle size distribution analysis. The authors would like to express their gratitude to Asta Nurmela, Taru Lehtikuusi, and Johanna Lukin of VTT for their experimental contributions. We acknowledge Jan Čapek and Efthymios Polatidis for their foundational work in developing the concept of PBF-LB/M processing for nickel-free duplex stainless steel and Tuomas Kantonen for his preliminary efforts in parameter screening, optimization, and printing of PBF-LB/M-built NiFDSS.

Prof. Ashish Ganvir acknowledges financial support from GREENBAT (Dnr 352517), co-funded by the Research Council of Finland and the European Union under the M-ERA.NET 2021 framework, as well as the SOLACE (Dnr 360540) Academy research fellowship, funded by the Research Council of Finland. He also extends his gratitude to the City of Turku for supporting his tenure-track grant. Prof. Antti Salminen acknowledges financial support through the DREAMS TEKN TOT (2600577911) project, funded by Business Finland. Zaiqing Que acknowledges the funding from the European Union –NextGenerationEU REPOWER NOVA project. We acknowledge the Materials Research Infrastructure (MARI) at the Department of Physics and Astronomy, University of Turku, for access and support with the SEM and XRD facilities.

Appendix A. Supplementary data

Supplementary data to this article can be found online at https://doi.org/10.1016/j.jmrt.2025.08.070.

References

[1] AL-Mangour B, Mongrain R, Irissou E, Yue S. Improving the strength and corrosion resistance of 316L stainless steel for biomedical applications using cold spray. Surf Coat Technol 2013;216:297–307. https://doi.org/10.1016/j.surfcoat.2012.11.061.
[2] Charles J. Corrosion resistance properties. Duplex stainless steels. 2013. p. 47–114. https://doi.org/10.1002/9781118557990.ch2.
[3] McGuire MF. Stainless steels for design engineers. ASM International; 2008. https://doi.org/10.31399/asm.tb.ssde.9781627082860.
[4] Patra S, Agrawal A, Mandal A, Podder AS. Characteristics and manufacturability of duplex stainless steel: a review. Trans Indian Inst Met 2021;74:1089–98. https://doi.org/10.1007/s12666-021-02278-7.
[5] Wang J, Uggowitzer PJ, Magdowski R, Speidel MO. Nickel-free duplex stainless steels. Scr Mater 1998;40:123–9. https://doi.org/10.1016/S1359-6462(98)00396-0.
[6] Anand A. Tribocorrosion behavior of novel nickel-free lean duplex stainless steel manufactured via laser-based powder bed fusion. https://doi.org/10.13140/RG.2.2.10310.08003; 2024.
[7] Sözen A, Neşer G. A critical systematic scoping review on the applications of additive manufacturing (AM) in the marine industry. Polymers 2025;17. https://doi.org/10.3390/polym17010004.
[8] Taş ŞO, Şener B. The use of additive manufacturing in maritime industry. Int J Eng Trends Technol 2019;67:47–51. https://doi.org/10.14445/22315381/IJETT-V67I6P209.
[9] Qi X, Liang X, Wang J, Zhang H, Wang X, Liu Z. Microstructure tailoring in laser powder bed fusion (L-PBF): strategies, challenges, and future outlooks. J Alloys Compd 2024;970:172564. https://doi.org/10.1016/j.jallcom.2023.172564.
[10] Zitelli C, Folgarait P, Schino A. Laser powder bed fusion of stainless steel grades: a review. Metals (Basel) 2019;9:731. https://doi.org/10.3390/met9070731.
[11] Salman OO, Gammer C, Chaubey AK, Eckert J, Scudino S. Effect of heat treatment on microstructure and mechanical properties of 316L steel synthesized by selective laser melting. Mater Sci Eng, A 2019;748:205–12. https://doi.org/10.1016/j.msea.2019.01.110.
[12] Xu M, Guo H, Wang Y, Hou Y, Dong Z, Zhang L. Mechanical properties and microstructural characteristics of 316L stainless steel fabricated by laser powder bed fusion and binder jetting. J Mater Res Technol 2023;24:4427–39. https://doi.org/10.1016/j.jmrt.2023.04.069.
[13] Vukkum VB, Gupta RK. Review on corrosion performance of laser powder-bed fusion printed 316L stainless steel: effect of processing parameters, manufacturing defects, post-processing, feedstock, and microstructure. Mater Des 2022;221:110874. https://doi.org/10.1016/j.matdes.2022.110874.
[14] Yin Y, Tan Q, Bermingham M, Mo N, Zhang J, Zhang M-X. Laser additive manufacturing of steels. Int Mater Rev 2022;67:487–573. https://doi.org/10.1080/09506608.2021.1983351.
[15] Xiang H, Zhao W, Lu Y. Effect of solution temperature on microstructure and mechanical properties of selective laser melted Fe–22Cr–5Ni-0.26N duplex

stainless steel. J Mater Res Technol 2022;19:1379–89. https://doi.org/10.1016/j.jmrt.2022.05.124.
[16] Hengsbach F, Koppa P, Duschik K, Holzweissig MJ, Burns M, Nellesen J, et al. Duplex stainless steel fabricated by selective laser melting - microstructural and mechanical properties. Mater Des 2017;133:136–42. https://doi.org/10.1016/j.matdes.2017.07.046.
[17] Nayak C, Anand A, Kamboj N, Kantonen T, Kajander K, Tupala V, et al. Tribological behavior and biocompatibility of novel nickel-free stainless steel manufactured via laser powder bed fusion for biomedical applications. Mater Des 2024;242:113013. https://doi.org/10.1016/j.matdes.2024.113013.
[18] Igual Munoz A, Espallargas N, Mischler S. In: Igual Munoz A, Espallargas N, Mischler S, editors. Tribocorrosion: definitions and relevance BT - tribocorrosion. Cham: Springer International Publishing; 2020. p. 1–6. https://doi.org/10.1007/978-3-030-48107-0_1.
[19] Qiu JH. Passivity and its breakdown on stainless steels and alloys. Surf Interface Anal 2002;33:830–3. https://doi.org/10.1002/sia.1460.
[20] Igual Munoz A, Espallargas N, Mischler S. In: Igual Munoz A, Espallargas N, Mischler S, editors. Tribocorrosion phenomena and concepts BT - tribocorrosion. Cham: Springer International Publishing; 2020. p. 35–42. https://doi.org/10.1007/978-3-030-48107-0_4.
[21] Stendal J, Fergani O, Yamaguchi H, Espallargas N. A comparative tribocorrosion study of additive manufactured and wrought 316L stainless steel in simulated body fluids. J Bio Tribocorros 2018;4:9. https://doi.org/10.1007/s40735-017-0125-9.
[22] Gao R, Liu E, Zhang Y, Zhu L, Zeng Z. Tribocorrosion behavior of SAF 2205 duplex stainless steel in artificial seawater. J Mater Eng Perform 2019;28:414–22. https://doi.org/10.1007/s11665-018-3791-y.
[23] Goel S, Bojinov M, Capek J, Saario T, Polatidis E, Kantonen T, et al. Corrosion behavior of laser powder bed fusion manufactured nickel-free stainless steels in high-temperature water. Corros Sci 2024;239:112410. https://doi.org/10.1016/j.corsci.2024.112410.
[24] Wu X, Liu J, Yang Y, Bai J, Shuai C, Buhagiar J, et al. Laser powder bed fusion of biodegradable magnesium alloys: process, microstructure and properties. Int J Extrem Manuf 2025;7. https://doi.org/10.1088/2631-7990/ad967e.
[25] Ling C, Li Q, Zhang Z, Yang Y, Zhou W, Chen W, et al. Influence of heat treatment on microstructure, mechanical and corrosion behavior of WE43 alloy fabricated by laser-beam powder bed fusion. Int J Extrem Manuf 2024;6. https://doi.org/10.1088/2631-7990/acfad5.
[26] Wang H, Li H, Wang J, Li F, Hu L. Microstructural evolution and strengthening mechanism in laser powder bed fusion 316L stainless steel with high strength and ductility. J Mater Eng Perform 2025;34:7426–36. https://doi.org/10.1007/s11665-024-09727-6.
[27] Sridhar N, Thodla R, Gui F, Cao L, Anderko A. Corrosion-resistant alloy testing and selection for oil and gas production. Corrosion Eng Sci Technol 2018;53:75–89. https://doi.org/10.1080/1478422X.2017.1384609.
[28] Pharr GM, Oliver WC. Measurement of hardness and elastic modulus by instrumented indentation: advances in understanding and refinements to methodology. J Mater Res 2004;19:3–20.
[29] Oliver WC, Pharr GM. Nanoindentation in materials research: past, present, and future. MRS Bull 2010;35:897–907. https://doi.org/10.1557/mrs2010.717.
[30] E01 Committee. Test methods for determination of carbon, sulfur, nitrogen, and oxygen in steel, iron, nickel, and cobalt alloys by various combustion and fusion techniques. West conshohocken, PA. 2018.
[31] Little B, Ray RI, Lee J. Understanding marine biocorrosion: experiments with artificial and natural seawater. Understanding Biocorrosion: Fundamentals and Applications 2014:329–40. https://doi.org/10.1533/9781782421252.3.329.
[32] Yuan X, Cai Y, Jiang J, Zhou Z, Wang C, Hu J, et al. Membrane-free osmotic desalination at near-room temperatures enabled by thermally responsive polyionic liquid hydrogels. J Mater Chem A 2022;10:24453–61. https://doi.org/10.1039/D2TA06869A.
[33] Practice S. ASTM-D1141-98-salt water. i:1–2, https://doi.org/10.1520/D1141-98R21.2; 2021.
[34] Kelly R, Scully J, Shoesmith D, Buchheit R. Electrochemical techniques in corrosion science and engineering. https://doi.org/10.1201/9780203909133; 2003.
[35] Astm. Standard practice for calculation of corrosion rates and related information, vol. 89. Astm G 102; 1999. p. 1–7. https://doi.org/10.1520/G0102-89R10.
[36] Ray SK, Banerjee A, Bhangi BK, Pyne D, Dutta B. 2 - tribological analysis—general test standards. In: George SC, Haponiuk JT, Thomas S, Reghunath R, Polymer Composites PS, Polymer Nanocomposites SBT-T of P, editors. Elsevier series on tribology and surface engineering. Elsevier; 2023. p. 17–50. https://doi.org/10.1016/B978-0-323-90748-4.00001-7.
[37] DeLong WT. A modified phase diagram for stainless steel weld metals. Metal Progress 1960;77:99–100B.
[38] Xavier CR, Junior HGD, De Castro JA. An experimental and numerical approach for the welding effects on the duplex stainless steel microstructure. Mater Res 2015;18:489–502. https://doi.org/10.1590/1516-1439.302014.
[39] Astafurov S, Astafurova E. Phase composition of austenitic stainless steels in additive manufacturing: a review. Metals (Basel) 2021;11. https://doi.org/10.3390/met11071052.
[40] Liu J, Wen P. Metal vaporization and its influence during laser powder bed fusion process. Mater Des 2022;215:110505. https://doi.org/10.1016/j.matdes.2022.110505.
[41] Pinto FC, Aota LS, Souza Filho IR, Raabe D, Sandim HRZ. Recrystallization in non-conventional microstructures of 316L stainless steel produced via laser powder-bed fusion: effect of particle coarsening kinetics. J Mater Sci 2022;57:9576–98. https://doi.org/10.1007/s10853-021-06859-1.
[42] Wang M, Xu T, Zhu Y, Yin W, Guo H, Zhao E, et al. Evolution of interface character distribution in duplex stainless steel processed by cross-rolling and annealing. J Mater Sci Technol 2018;34:2160–6. https://doi.org/10.1016/j.jmst.2018.02.018.
[43] Zhang L, Liu L, Liu F, Sun J, Wang D. Effect of post-heat treatment on the mechanical properties and corrosion behavior of duplex stainless steel fabricated by wire arc additive manufacturing. Arch Metall Mater 2024;69:667–74. https://doi.org/10.24425/amm.2024.149796.
[44] Gadelrab KR, Li G, Chiesa M, Souier T. Local characterization of austenite and ferrite phases in duplex stainless steel using MFM and nanoindentation. J Mater Res 2012;27:1573–9. https://doi.org/10.1557/jmr.2012.99.
[45] Spierings AB, Herres N, Levy G. Influence of the particle size distribution on surface quality and mechanical properties in AM steel parts. Rapid Prototyp J 2011;17:195–202. https://doi.org/10.1108/13552541111124770.
[46] Feng H, Dai J, Li H, Cao X, Zhu H, Zhang S, et al. Visualizing and quantifying the influence of N-Mo synergy on corrosion resistance of stainless steel by dissolution-diffusion-deposition model. Corros Sci 2024;235:112162. https://doi.org/10.1016/j.corsci.2024.112162.
[47] Tian H, Wang J, Liu Z, Han P. Effect of nitrogen on the corrosion resistance of 6Mo super austenitic stainless steel. Metals (Basel) 2024;14. https://doi.org/10.3390/met14040391.
[48] Vats V, Baskaran T, Arya SB. Tribo-corrosion study of nickel-free, high nitrogen and high manganese austenitic stainless steel. Tribol Int 2018;119:659–66. https://doi.org/10.1016/j.triboint.2017.11.023.
[49] Tütük İ, Ural MM, Özer G, Kisasöz A. Influence of solution treatment process on the properties of duplex stainless steels: a comparative study on microstructure and corrosion properties of UNS S32205 and UNS S32760. Metall Mater Trans B 2024;55:2916–21. https://doi.org/10.1007/s11663-024-03154-7.
[50] Pan J. Studying the passivity and breakdown of duplex stainless steels at micrometer and nanometer scales – the influence of microstructure. Front Mater 2020;7. https://doi.org/10.3389/fmats.2020.00133.
[51] Abreu D, Silva WM, Ardila MAN, De Mello JDB. Tribocorrosion in ferritic stainless steels: an improved methodological approach. Mater Res 2022;25. https://doi.org/10.1590/1980-5373-MR-2021-0179.
[52] Biezma MV, Martin U, Linhardt P, Ress J, Rodríguez C, Bastidas DM. Non-destructive techniques for the detection of sigma phase in duplex stainless steel: a comprehensive review. Eng Fail Anal 2021;122:105227. https://doi.org/10.1016/j.engfailanal.2021.105227.
[53] Hou B-X, Sheu H-H, Lin M-Y, Lee C-Y, Lee H-B. Corrosion and wear behavior of 17-4PH stainless steel manufactured by selective laser melting and bulk material after solution treatment. Coatings 2025;15. https://doi.org/10.3390/coatings15060649.
[54] Weinberger C, Boyce B, Battaile CC. Slip planes in bcc transition metals. Int Mater Rev 2013;58:296–314. https://doi.org/10.1179/1743280412Y.0000000015.
[55] Xin J, Zhang H, Sun W, Wang W, Wu D, Lyu B, et al. Microstructure evolution of austenitic stainless steels under high-cycle-fatigue loading at deep cryogenic temperature. Scr Mater 2023;226:115223. https://doi.org/10.1016/j.scriptamat.2022.115223.
[56] Ashby MF, Lim SC. Wear-mechanism maps. Scripta Metall Mater 1990;24:805–10. https://doi.org/10.1016/0956-716X(90)90116-X.
[57] Fargas G, Mestra A, Mateo A. Effect of sigma phase on the wear behavior of a super duplex stainless steel. Wear 2013;303:584–90. https://doi.org/10.1016/j.wear.2013.04.010.
[58] Tribology. Materials and surface engineering in tribology. 2008. p. 49–108. https://doi.org/10.1002/9780470611524.ch2.